

## Article

# Lithium-Ion Batteries (LIBs) Immersed in Fire Prevention Material for Fire Safety and Heat Management

Junho Bae <sup>1</sup>, Yunseok Choi <sup>1</sup> and Youngsik Kim <sup>1,2,\*</sup> 

<sup>1</sup> School of Energy and Chemical Engineering, Ulsan National Institute of Science and Technology (UNIST), Unist-gil 50, Ulsan 44919, Republic of Korea; juno@unist.ac.kr (J.B.)

<sup>2</sup> R&D Center, 4TOONE Corporation, UNIST-gil 50, Ulsan 44919, Republic of Korea

\* Correspondence: ykim@unist.ac.kr

**Abstract:** Lithium-ion batteries (LIBs) have emerged as the most commercialized rechargeable battery technology. However, their inherent property, called thermal runaway, poses a high risk of fire. This article introduces the “Battery Immersed in Fire Prevention Material (BIF)”, the immersion-type battery in which all of the LIB cells are surrounded by a liquid agent. This structure and the agent enable active battery fire suppression under abusive conditions while facilitating improved thermal management during normal operation. Abuse tests involving a battery revealed that the LIB module experienced fire, explosions, and burnouts with the target cell reaching temperatures of 1405 °C and the side reaching 796 °C. Conversely, the BIF module exhibited a complete lack of fire propagation, with temperatures lower than those of LIBs, particularly 285 and 17 °C, respectively. Under normal operating conditions, the BIF module exhibited an average temperature rise ~8.6 times lower than that of a normal LIB. Furthermore, it reduced the uneven thermal deviation between the cells by ~5.3 times more than LIB. This study provides a detailed exploration of the BIF and covers everything from components to practical applications. With further improvements, this technology can significantly enhance fire safety and prevent the thermal degradation of batteries in the real world.

**Keywords:** lithium-ion battery; liquid immersion battery; battery thermal management system; thermal runaway propagation; energy storage system



**Citation:** Bae, J.; Choi, Y.; Kim, Y.

Lithium-Ion Batteries (LIBs)

Immersed in Fire Prevention Material  
for Fire Safety and Heat Management.

*Energies* **2024**, *17*, 2418.

<https://doi.org/10.3390/en17102418>

Academic Editors: Andrea Trovò and  
Walter Zamboni

Received: 18 April 2024

Revised: 7 May 2024

Accepted: 15 May 2024

Published: 17 May 2024



**Copyright:** © 2024 by the authors. Licensee MDPI, Basel, Switzerland. This article is an open access article distributed under the terms and conditions of the Creative Commons Attribution (CC BY) license (<https://creativecommons.org/licenses/by/4.0/>).

## 1. Introduction

Lithium-ion batteries (LIBs) are the most widely commercialized battery technology for their exceptional electrochemical performances, including high energy density and power [1]. However, due to the risk of a characteristic called thermal runaway, fires often occur under harsh conditions (high temperature, high C-rate) or in abnormal environments (improper thermal management) regardless of their application, such as in electric vehicles (EVs), energy storage systems (ESSs), and smart devices [2,3]. These fire incidents arise from the convergence of three factors: heat (exothermic chain reactions to reach the ignition point), combustible components (battery electrolytes and separators), and the presence of oxygen [4–6].

Various solutions, such as battery thermal management systems, fire suppression agents, and devices, have been developed to address this problem. Representative solutions are technologies that disrupt battery–oxygen contact and cool the batteries to prevent temperatures from reaching the ignition point [7]. To mitigate oxygen contact, fire suppression materials such as hydrofluorocarbon (HFC) [8–10], solid aerosol K<sub>2</sub>CO<sub>3</sub> [11,12], and ABC powder [13] are installed within battery modules or rack systems to suffocate the fire by chemically reacting with oxygen [4,5,13]. For cooling, fire-extinguishing systems are under development, which involve injecting or spraying agents such as Novec 1230 [14,15] or liquid nitrogen [16,17]. These conventional agents can absorb substantial amounts of heat because of their latent heat of evaporation.

However, these methods react only after a fire has already occurred [18]. Owing to the characteristics of battery fires that result in high-energy explosions in random cells, extinguishing fires using conventional agents installed within a system poses challenges. Moreover, in the case of modules or packs in contact with high-density LIB cells, such as ESSs, the speed and scale of fire propagation increase rapidly, further exacerbating the extinguishment [19,20].

To improve the fire suppression performance, the research around immersing the batteries into cooling agents is recently in development. This method not only enables thermal management at all times, as all of the batteries are immersed in the agent, but also overcomes the disadvantage of existing solutions through the immediate agent penetration into the thermal runaway cell. However, the selection of suitable fire-extinguishing agents for conventional immersion-type batteries is limited [21–23] because they should not cause corrosion or conductivity issues when in contact with the batteries. The conventional agents, used in immersion-type batteries, have incomplete fire-extinguishing capabilities due to slow heat dissipation caused by low thermal conductivity and heat capacity [9,15,22]. Also, safety concerns are prevalent [21]. So, they are used only to prevent fires through thermal management instead of extinguishing them [24]. Some researchers have developed water-based extinguishing agents [24] that have a better cooling effect than conventional agents; but due to the problems that occur during the immersion mentioned, they were developed only in the form of mist or injections [21,23].

Therefore, we expanded the selection range of fire-extinguishing agents by applying hermetical sealing to the batteries, capable of making batteries safe from the agent, and devised the “Battery Immersed in Fire Prevention Material (BIF)”. In the BIF, all cells within the battery operate while fully submerged in the liquid agent solution, which has an outstanding fire suppression performance through high thermal conductivity and heat capacity. It immediately suppresses fires during abusive conditions and provides enhanced electrochemical performance during normal operation through heat management.

As shown in Figure 1, this study covers the components of the practical applications of BIF.

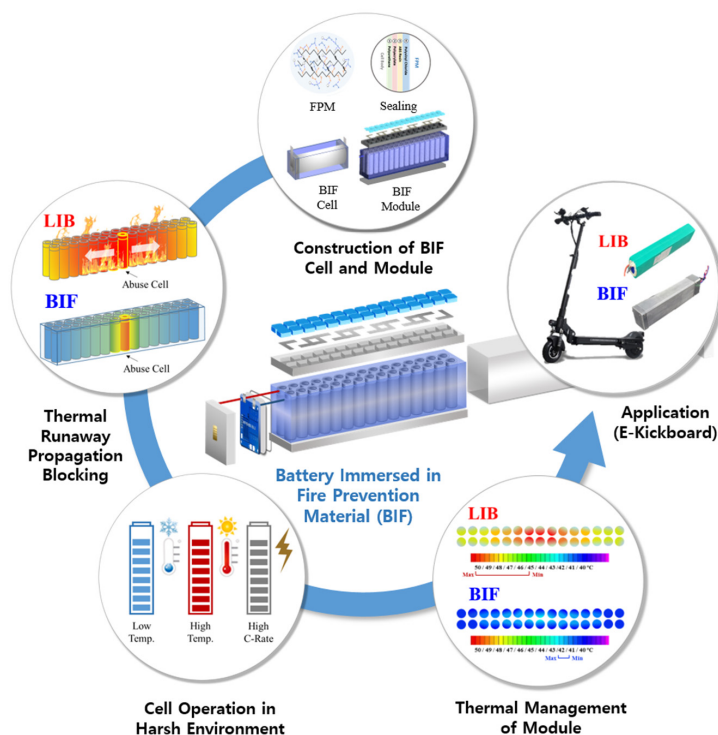


**Figure 1.** Configuration of the battery immersed in fire prevention material (BIF) and research from the construction of the battery to application in sequence.

First, the study explains the components of BIF, such as FPM and sealing materials. The BIF cell and module used for the experiments are designed with these functional components. Second, the single cell at the center of the BIF module was intentionally overheated to test its fire-propagation prevention capabilities, which were compared with those of the LIB module under identical conditions. Third, the performances of cycle life, capacity, Electrochemical Impedance Spectroscopy, maximum discharge C-rate, and temperatures of the BIF are compared with LIB in harsh operating conditions to verify the thermal management effect.

The BIF is a solution for immediate fire suppression and thermal management simultaneously, surpassing the conventional fire suppression methods. This study is expected to contribute to the applications of BIF in the real world such as mobility (e.g., kickboards), ESSs (energy storage systems), and EVs [25].

## 2. Materials and Methods

In the Materials and Methods Section, components of the BIF, BIF cell, and module used for the experiments and the experiment conditions are explained.

### 2.1. Components of the BIF

#### 2.1.1. Lithium-Ion Battery (LIB) Cell

The cylinder (18650) type of lithium-ion battery cells (model number: INR18650-30Q) was used in the BIF module. Because cylindrical cells exhibit a lower volume than prismatic or pouch-type cells, constructing modules of diverse shapes and specifications considering series or parallel connections is simple. In this study, 30 LIB cells comprised a BIF module connected in 10s3p and fastened in a  $15 \times 2$  array for application in an electric kickboard (EV).

#### 2.1.2. Fire Prevention Material (FPM)

FPM surrounds the lithium-ion battery via immersion, and this agent is applied in BIF for the fire suppression and thermal management of the batteries. It immediately penetrates into the lithium-ion battery and suppresses fires under abusive conditions. Also, it provides enhanced electrochemical performance during normal operations through effective heat management.

The components of the FPM were selected to have high cooling and oxygen-blocking efficiency. The main component of the material, the water [26] occupying 94% of the FPM, absorbs the heat for thermal management. It has the advantages of heat capacity, high accessibility, manageable treatment, and low cost. The PVA (polyvinyl alcohol) chain, occupying 4% of the FPM, prevents water evaporation and blocks oxygen. Boric acid regulates the pH, and the Sodium Bicarbonate helps the crosslinking of the agents. Additionally, the expanded glass powder is added for film layer coating to the battery at a high temperature ( $\sim 650$  °C) to block the oxygen. When the thermal runaway happens, the FPM starts to absorb the heat and evaporate. After the whole of the water molecule evaporates over 100 °C, the polymer and powder in FPM coat the oxygen-blocking films to the battery. The synthesis method of the FPM is described in the Supporting Materials. Also, the detailed fire suppression process and flame-retardant performances of the FPM are described in Figure S1.

Figure 2a shows the structure and material composition of the FPM applied to the BIF. The polyvinyl alcohol (PVA) chain constructed the backbone of the material, and molecules such as water, boric acid, and fumed silica were crosslinked within. The hydrophilic PVA chain fixes the water molecules and the rest molecules form linkages with each other through hydrogen bonds.

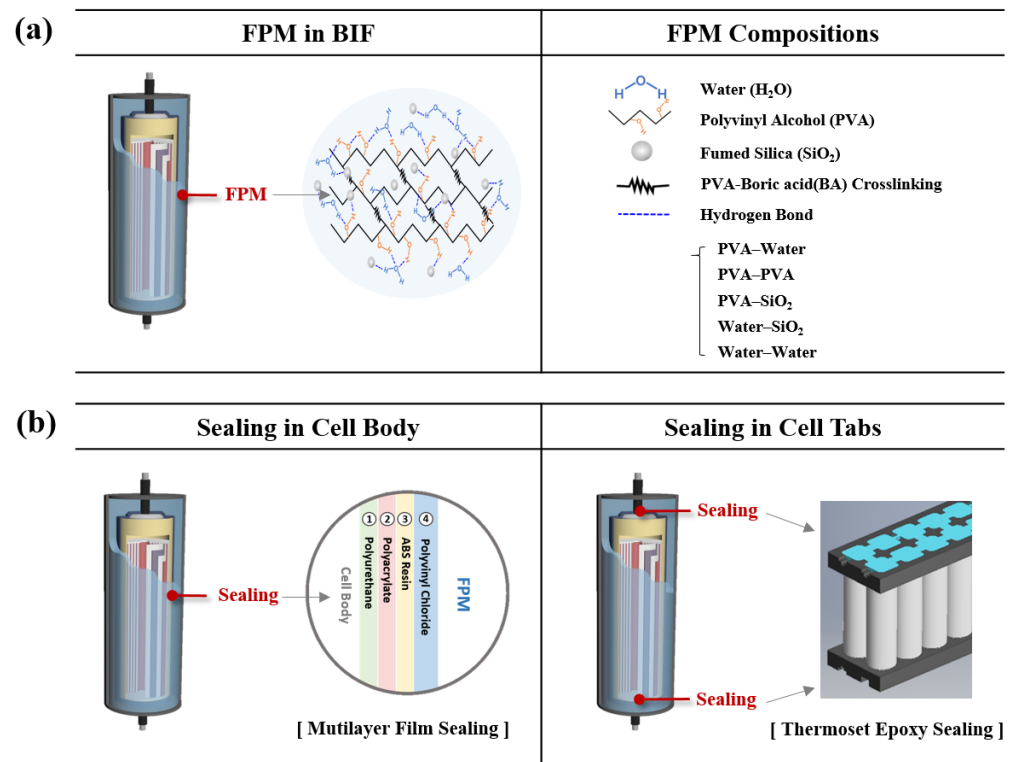


**Figure 2.** Functional components of BIF: (a) structure and composition of fire prevention material (FPM) immersing the battery, and the application of (b) sealing within the cell body and cell tabs to prevent direct contact of FPM to the battery.

The properties of the FPM are suited for immersion-type batteries [27]. It exhibits a high heat conductivity ( $0.559 \text{ W m}^{-1} \text{ K}^{-1}$ ), heat transfer coefficient (about  $1000 \text{ W m}^{-2} \text{ }^\circ\text{C}^{-1}$ ), density ( $0.94 \text{ kg m}^{-3}$ ), heat capacity ( $3.92 \text{ J g}^{-1} \text{ }^\circ\text{C}^{-1}$ ), and latent heat energy ( $2125 \text{ J g}^{-1}$ ). Due to the high heat conductivity and heat transfer coefficient, FPM can more efficiently absorb the heat emitted from batteries during operation and thermal runaway than the conventional agents as Table S1. At the same time, the high density, heat capacity, and latent heat energy prevent large temperature increases in FPM. The superior material properties of FPM are compared with the other battery fire suppression agents in Table S1.

For the next step, to determine the appropriate quantity of FPM to be incorporated into the BIF, the theoretical amount of FPM required to block the fire was calculated. First, the maximum heat energy generated with the LIB short circuit was calculated (Equation (1)). It differs based on the material and type of cell but is usually proportional to the energy of the battery [28,29].

The heat absorbance of the FPM was then calculated as the sum of the heat required to increase the temperature and the latent heat (Equation (2)). The heat capacity ( $3.92 \text{ J g}^{-1} \text{ }^\circ\text{C}^{-1}$ ) and the temperature difference from room temperature (RT) to the boiling point of the water ( $100 \text{ }^\circ\text{C}$ ) were calculated. Because the thermal runaway temperature is higher than the boiling point of the FPM, the latent heat of the FPM ( $2261 \text{ J g}^{-1}$ ) is considered. Assuming that the energy generated from the short circuit is entirely converted into heat at the room temperature of  $25 \text{ }^\circ\text{C}$ , Equations (1) and (2) yield the same values. Consequently, the  $1.48 \text{ g/Wh}$  of FPM was applied to BIF. The experiments for verifying these calculations of the required theoretical amount of FPM and its fire suppression performance are performed in Figure S2.

$$E(\text{Wh}) \times 3600 \frac{\text{J}}{\text{Wh}} = Q(\text{kJ}) \quad (1)$$

$$3.92 \frac{\text{kJ}}{\text{kg} \cdot \text{ }^\circ\text{C}} \times m \times (100 - RT) \text{ }^\circ\text{C} + 2.261 \frac{\text{kJ}}{\text{g}} (Q_{\text{FPM, Latent}}) \quad (2)$$

### 2.1.3. Sealing

Nonetheless, because the primary component of the FPM is water, it exhibits high electrical conductivity. Directly submerging the battery into the FPM results in severe damage, connecting the anode and cathode. The material to prevent direct contact with the battery and the FPM should be applied between them.

Therefore, sealing was applied to the BIF to prevent ingress of FPM from the battery under normal conditions. Simultaneously, it facilitates FPM penetration into the cell through tearing when abuse, such as thermal runaway, occurs. To perform these functions, the sealing should be sufficiently thin for effective thermal conductance during operation and allow direct FPM penetration into the cell for early fire blocking. In addition, to protect cells that would suffer damage from FPM under normal conditions, such as a short circuit due to moisture, the Water Vapor Transmission Rate (WVTR) should be low. Considering these conditions, the sealing covers the entire battery surface and is divided into two parts: the cell body and cell tabs. For effective heat conductance and preventing moisture penetration into the battery, the thin (0.22 mm) and very low WVTR (0.1 g/m<sup>2</sup> day) multilayer films composed of polyurethane, polyacrylate, ABS resin, and polyvinyl chloride were applied to the cell bodies, as shown in Figure 2b. Cell tabs, however, require a higher level of sealing than the cell body because of the Ni tab connections in the cell tabs and the sophisticated structure of the cell holder. Therefore, a highly transformable thermoset epoxy (Epons ES-2) with 2.0 mm thickness with WVTR (0.5 g/m<sup>2</sup> day) was applied to the cell tabs.

### 2.1.4. The Else Components

Cell holders were applied to the tabs of the battery cell in the module. They were developed to fix an array of cells and maintain uniform distances between the cells. Furthermore, they were designed to fill the epoxy sealing after spotting nickel tabs onto the cell tabs. In addition, it helps the cells to be immersed in the FPM during operation and under abusive conditions through fixation.

The BMS controls the safety functions, including overdischarge, overcharging, overcurrent, and balancing. It was applied in the BIF module.

The I/O terminal (input and output terminal) was applied to the end of the BIF tab for charging and discharging the battery module with an adequate current.

The case was designed to house all of the BIF components in a single unit, called the BIF cell and module. In the BIF cell case, a single LIB cell with epoxy-sealed tabs was immersed in the FPM. In this BIF module case, 30 LIB cells with cell holders and epoxy-sealed tabs were immersed in the FPM.

## 2.2. BIF Cell and Module

The BIF cell is designed to estimate the electrochemical performances, compared with LIB in harsh operating conditions. For effective fire suppression and thermal management, the immersion fluid (FPM) was regularly brought into contact with the cell body and sealed with multilayer films. The 16.4 g of FPM was brought into contact with the cell at 2 mm intervals from the case, occupying 28% of the total module weight.

The BIF module is designed to have multiple battery cells to measure the heat deviation between the cells in harsh operating conditions and numerically estimate the degree of the blocking of fire propagation when thermal runaway occurs. For effective fire suppression and thermal management, the immersion fluid (FPM) was regularly inserted between all the cells in the module. The 492 g of FPM was inserted into the cells in the BIF module at 2 mm intervals, occupying 21% of the total cell weight.

Figure 3 illustrates the construction and components of the BIF cell and module. It comprises the LIB cell and the functional components of the BIF such as the FPM, sealing, and selectively the other components such as the cell holder, case, BMS, I/O terminal, and Ni tab that allow operation. Tables 1 and 2 provide the specifications of the BIF cell and

module, together with its electrochemical parameters [30], such as the battery, BMS, and operating conditions [27,31,32].

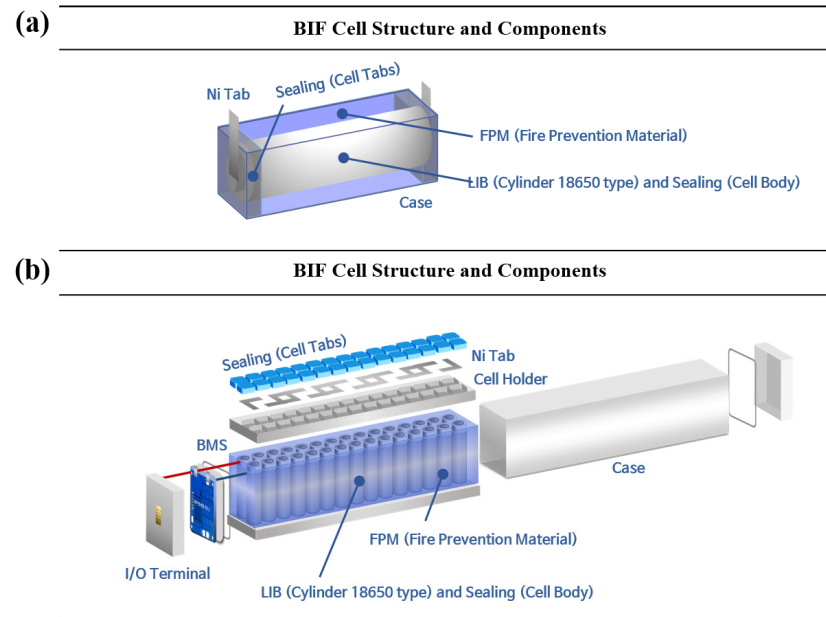


**Figure 3.** Overview of the (a) BIF cell and (b) BIF module with their components and structure.

**Table 1.** Specification of the BIF Cell.

Parameters		Description
Battery	Cell	LIB 18650 type
	Cell Manufacturer	Samsung
	Cell Model	INR18650-30Q
	Nominal Voltage	3.7 V
	Maximum Voltage	4.2 V
	Capacity	3 Ah
Charge	Energy	11 Wh
	Maximum Charge Voltage	4.2 V
	Continuous Charging Current	1.5 A
Discharge	Maximum Discharge Voltage	3.0 V
	Continuous Discharge Current	1.5 A
	Others	
	Dimension (B × W × H)	26 mm × 79 mm × 26 mm
	Total Weight (FPM Weight)	58.5 g (FPM: 16.4 g)
	Operating Temperature	−10–40 °C

**Table 2.** Specification of the BIF Module.

Parameters		Description
Battery	Cell	LIB 18650 type (10s3p)
	Cell Manufacturer	Samsung
	Cell Model	INR18650-30Q
	Nominal Voltage	37 V
	Maximum Voltage	42 V
	Capacity	9 Ah
Charge	Energy	333 Wh
	Maximum Charge Voltage	42 V
	Continuous Charging Current	4.5 A

Table 2. Cont.

Parameters	Description
Discharge	Maximum Discharge Voltage Continuous Discharge Current
	30 V 4.5 A
Others	Dimension (B × W × H) Total Weight (FPM Weight) Operating Temperature
	45 mm × 350 mm × 80 mm 2.8 kg (FPM: 492 g) −10–40 °C
Battery Management System	Function
	Over-discharge, Overcharge, Over-current, Balance, etc.

### 2.3. Experiment Conditions

#### 2.3.1. Thermal Management

To estimate the thermal management performance of the BIF, its electrochemical performances, such as capacity, cycle, Electrochemical Impedance Spectroscopy (EIS), and voltage efficiency, were compared with those of the LIB. All experiments were conducted under harsh conditions (high/low temperature and high current) to imitate the application operation and abuse conditions [33]. The operating temperature was  $\sim 40$  °C, the charge current was 1 C, the discharge current was 3C/4C, and the voltage cut was 2.8 V/4.2 V. Thermocouples were attached at uniform locations, the center of the cell body, for all the experiments to record the temperatures.

#### 2.3.2. Thermal Runaway Propagation

To estimate the fire stability of the BIF module, thermal runaway propagation tests were compared with those of the LIB module as Figure 4. The abuse was induced by overheating a single cell at the center of the module. The trigger cell was wound with a Ni-Cr heating coil, and the maximum sustained temperature was  $\sim 350$  °C by the power supply. The voltages of the module and the temperature in diverse spots were measured using a data logger. All the experiments were conducted in an explosion-proof chamber for safety purposes.

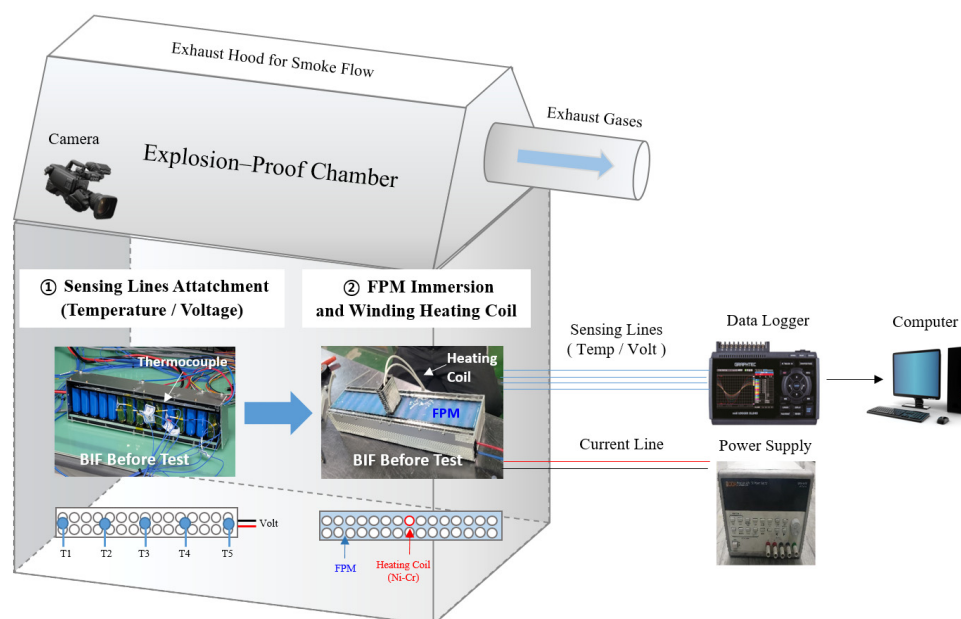


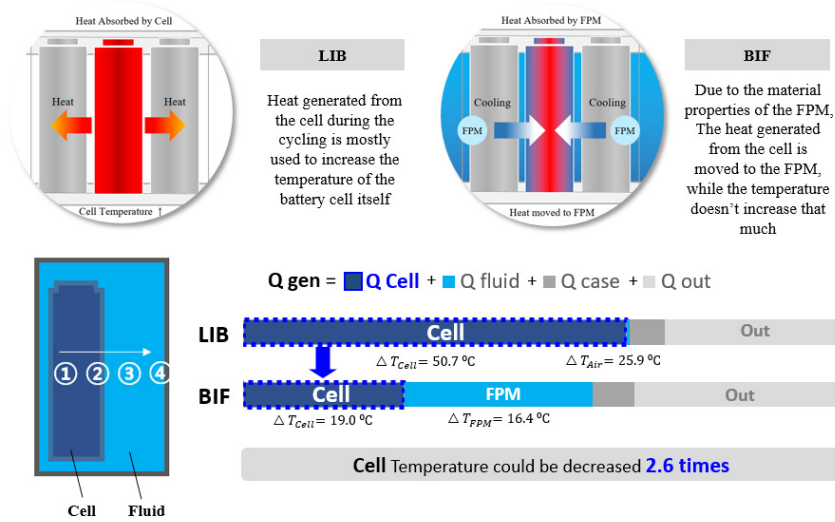
Figure 4. Setup and preparation for the abuse test (overheating) of the BIF module.

### 3. Results and Discussion

#### 3.1. Mechanism and Heat Transmission Diagram with the Governing Equations

Before the test, the mechanisms through which the FPM on the cell surface in the BIF absorbs heat compared to LIB during thermal management and fire suppression are represented. Then, the process of how the heat generated from the battery cell dissipates and the absorption heat amount of each component are calculated. The 3.7 V/3 Ah/18,650 type cell was used, and the theoretical amount(1.48 g/Wh) of fluid was applied. Thermal management was estimated in harsh conditions (40 °C/3C Discharge and 1C Charge), and the thermal propagation was induced by overheating the cell at 350 °C. Before the abuse test and electrochemical performance estimation in the real environment, the thermal behavior of the LIB and BIF was simulated using the ANSYS Fluent Multiphysics Computational Fluid Dynamics (CFD) simulator in Figure 5. The fluid of LIB is the air, and the fluid of the BIF is the FPM in both thermal management and thermal runaway propagation. The mechanisms and governing equations are as follows.

##### (a) Thermal Management (Cycling)



##### (b) Thermal Runaway Propagation Prevention

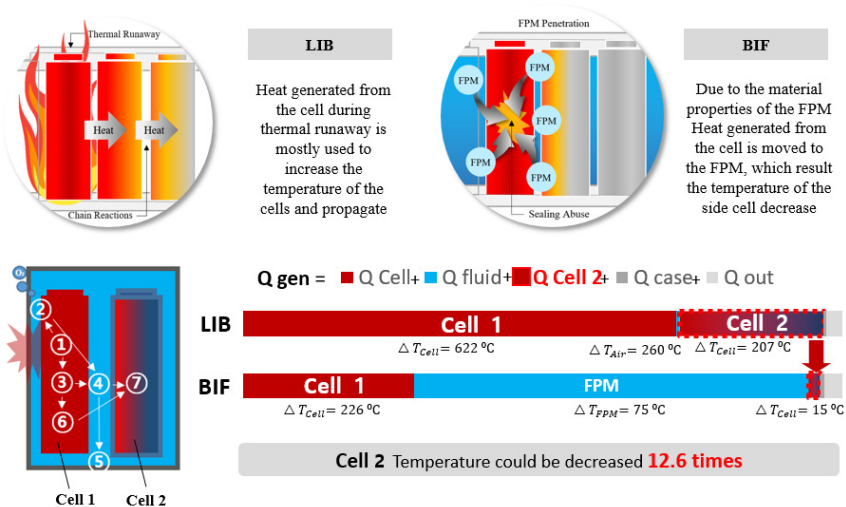


**Figure 5.** Configuration of the mechanisms comparison of the LIB and BIF with heat transmission sequence and the direction of the heat distributions during (a) thermal management under normal operating conditions and (b) thermal runaway propagation under abusive conditions.

In Figure 5a, the mechanism by which the FPM on the cell surface in the BIF absorbs heat during thermal management is described below. It shows the direction of heat transmission from the battery to the outside. Rapid heat transfer and small temperature increases are important for efficient heat management [28,29]. Equation (3) expresses the energy conservation related to electrochemistry and thermodynamics. The following parameters were used for the equation:  $\rho_b$ , the density of the battery ( $\text{kg m}^{-3}$ );  $C_{p,b}$ , the heat capacity of the battery ( $\text{J kg}^{-1}\text{K}^{-1}$ );  $T_b$ , the temperature of the battery (K);  $k_b$ , the thermal conductivity of the battery ( $\text{W m}^{-1}\text{K}^{-1}$ ); and  $Q_{Gen}$ , the heat generation of the battery (W) [31,32].

Related to this equation, the heat generated by the battery can be divided into irreversible and reversible heat (Equation (4)). Irreversible heat is generated from the resistance caused by the electron or ion transmission (Equation (5)). It could be driven by the ohmic losses in the battery ( $\eta\Omega$ ), the diffusion and migration of Li ions through the electrolyte ( $\eta m$ ), the diffusion of the Li-ion inside the electrodes ( $\eta d$ ), and the charge transfer reactions at the electrode/electrolyte interface ( $\eta ct$ ) (Equation (6)). Reversible heat is generated from entropy changes in the electrodes through electrochemical reactions (Equation (7)).

$$\textcircled{1} \text{ Batteries} = \rho_b c_{p,b} \frac{\partial T_b}{\partial t} = \nabla \cdot (k_b \nabla T_b) + Q_{Gen} \quad (3)$$

$$Q_{Gen} = Q_{irrev} + Q_{rev} \quad (4)$$

$$Q_{irrev} = I\eta_{total} = I(E - E_{eq}) = I^2 R_{int} \quad (5)$$

$$\eta t = E - E_{eq} = \eta\Omega + \eta m + \eta d + \eta ct \quad (6)$$

$$Q_{rev} = -\frac{IT \Delta S}{nF} = -IT \left( \frac{\partial E_{eq}}{\partial T} \right) SoC, \quad \Delta S = nF \left( \frac{\partial E_{eq}}{\partial T} \right) SoC \quad (7)$$

Subsequently, heat from the battery is applied to the sealing layer using Fourier's law (Equation (8)). Additionally, heat is transferred to the FPM, which has a heat transfer coefficient  $\sim 500$  times higher than that of air, according to Newton's law (Equation (9)) [30,31]. So, the FPM can absorb a lot more heat from the battery cell than air.

$$\textcircled{2} \text{ Contact Surface} = -k_{battery} A \frac{\partial T}{\partial n} = -k_{sealing, FPM} A \frac{\partial T}{\partial n} \quad (8)$$

$$= -k_{battery} A \frac{\partial T}{\partial n} = h_{FPM} A (T_{battery} - T_{FPM}) \quad (9)$$

The energy conservation of the FPM is expressed in Equation (10). Because it does not include latent heat or flow, the equation can be simplified.

$$\textcircled{3} \text{ FPM} = \rho_{FPM} c_{p,FPM} \frac{\partial T_b}{\partial t} = \nabla \cdot (k_{FPM} \nabla T_b) \quad (10)$$

Lastly, the heat dissipation equation includes the parameters of  $T_b$ : the temperature of the battery (K) and  $\partial T/\partial n$ : the temperature gradient for heat emission (Equation (11)).

$$\textcircled{4} \text{ Heat Dissipation} = -k_{2,FPM} \frac{\partial T}{\partial n} = h(T_{FPM} - T_{amb}) \quad (11)$$

Owing to the significantly greater heat capacity of FPM compared to air (about 4 times) and its elevated heat transfer coefficient and density (about 1000 times), it can absorb the heat emanating from the battery efficiently while the temperature of the FPM does not increase that much. This resulting temperature of the BIF cell could be decreased about 2.6 times more than LIB.

Figure 5b illustrates the heat transfer mechanism during thermal runaway in a single-module cell. The principle of transferring the heat generated from the battery to adjacent cells or outside the cell was established sequentially using formulas. To prevent propagation, it is important to decrease the heat reaching the side cells [32]. The heat generated

during thermal runaway was divided into released energy and accumulated energy, which were used to increase the cell temperature (Equation (12)).

$$\begin{aligned} \textcircled{1} \text{ Heat Generated during thermal abuse} \\ = \text{Combustion Heat Release (CHR) + Heat Accumulation (HA)} \end{aligned} \quad (12)$$

The energy emitted to the outside of the battery module, called CHR, can be calculated using  $E$ , combustion heat released per unit mass of ( $=13.1 \times 10^3 \text{ kJ kg}^{-1}$ ); and  $m$ , mass flow of oxygen ( $\text{kg s}^{-1}$ ) (Equation (13)).

$$\textcircled{2} \text{ CHR} = E \left( m_{O_2, flow in} - m_{O_2, flow out} \right) \quad (13)$$

HA can be calculated using Equation (14), which shows the heat distribution inside the module:

$$\textcircled{3} \text{ HA} = cb \sum_{i=1}^n m_i b(T_{i, max} - T_0) \quad (14)$$

The heat then moves from the cell to the FPM, and (15) expresses the heat absorbance ability of the sensible and latent heat of the FPM. The equation was divided into the heat capacity required to increase the temperature itself (Equation (16)) and the latent heat used for the phase change, which is proportional to the ratio of water (Equation (17)) [33,34].

$$\textcircled{4} \text{ FPM Heat Absorbance [J]} = Q_{FPM, Sensible} + Q_{FPM, Latent} \quad (15)$$

$$Q_{FPM, Sensible} = C_{p, FPM} \cdot m_{FPM} \cdot \Delta T_{FPM} \quad (16)$$

$$Q_{FPM, Latent} = Q_{Water, Latent} \cdot 0.946 = r_{water} \cdot m_{water} \quad (17)$$

Finally, the heat exiting the battery can be expressed using Equation (18).

$$\textcircled{5} \text{ Heat Out} = Q_{Cell, Out} = h \cdot A_{Cell} \cdot T_{(Cell-air)} \quad (18)$$

Immediately after the thermal runaway, the residual heat inside the battery module can be expressed as Equation (19):  $A_r$ , the battery cross-sectional area, and  $T_i(y)$ , the axial temperature distribution of the batteries, are the required parameters. The relationship between the heat dissipation of the battery module ( $H_{dis}$ ), the heat accumulated at the beginning of the FPM reaction ( $HA_{start}$ ), and the thermal runaway heat generated during FPM application ( $HA_{TR}$ ) can be written as Equations (20) and (21).

$$\textcircled{6} \text{ HA}_{re} = \sum_{i=1}^n \int \rho_b A_r c_b (T_i(y) - T_0) dy \quad (19)$$

$$H_{dis} = HA_{start} - HA_{re} + HA_{TR} \quad (20)$$

$$HA_{TR} = \sum m_{i,b} c_b (T_{i, max} - T_{i, start}) \quad (21)$$

Finally, thermal runaway propagation occurred when the temperature and heat exceeded the critical temperature point ( $c1$ ). The parameters used for Equation (22) are  $C1$ , critical control temperature for the battery module (K);  $C2$ , critical control temperature for a single battery (K);  $P_h$ , battery heating power (W);  $P_t$ , heat transfer power (W);  $P_b$ , FPM cooling power on a single battery (W); and  $F_c$ , cooling factor (to determine the inflection point).

$$\textcircled{7} \text{ TRP when } \int_{Tc1}^{Tc2} c_b m_b dT \leq \int_{t(Tc1)}^{t(Tc2)} (P_h + P_t - P_b) dt \quad (22)$$

To summarize, when thermal runaway happens, an abundant amount of heat (about 17 times) is generated in a short time (about 0.002 times) compared to thermal management. The FPM can efficiently absorb the heat generated from the thermal runaway cell than air

as the heat absorbance is 2432 J/g, and 1 J/g each. This resulting temperature of the side cell of BIF could be decreased by about 12.6 more times than LIB.

### 3.2. Thermal Runaway Propagation Test

To estimate and compare thermal runaway propagation between the LIB module and the BIF module, a single cell in the center of the module was overheated to induce thermal runaway [34–36]. For overheating, the heating coil, composed of nickel and chromium, was wound to the abuse cell and heated over 350 °C using the power supply equipment. The temperatures and voltage of the modules were recorded to estimate the thermal runaway propagation scale, and the temperature-sensing lines called thermocouples were attached to the cell body at the center of the module and the side parts of the module. The results of step time to lead thermal runaway, sudden temperature increase, and propagated cell amount are numbered in Table 3, when thermal runaway occurred via target cell abuse and propagations. In the LIB module, the abuse cell drove thermal runaway propagation step-by-step [37,38], and finally, all the cells suffered exhaustion [39]. However, direct FPM penetration into the abuse target cell in the BIF module prevents extensive propagation. The thermal runaway reactions of the battery by stage are described specifically in Figure S3.

**Table 3.** Step Time Intervals, Abrupt Temperature Rises, and Propagated Cell Amount while Thermal Runaway Occurs in LIB and BIF Module.

Thermal Runaway		①	②	③	④
LIB	Step Time (s)	377	134	46	30
	$\Delta T$ (°C)	152.9	163.1	741.1	900.3
	Propagated Cell Amount	1 ea (Abuse)	1 ea	5 ea	6 ea
BIF	Step Time (s)	396	129	-	-
	$\Delta T$ (°C)	110.0	113.1	-	-
	Propagated Cell Amount	1 ea (Abuse)	1 ea	-	-

Figure 6a shows the temperatures and voltages of the LIB module with respect to time. When heat accumulated and the temperature of the abuse cell increased over 100 °C, the abuse cell suffered a thermal runaway. The sudden temperature increase was ~153 °C, while the abuse happened within 377 s. The module experienced a large fire with an explosion. Thereafter, continuous fire led to the propagation of TR to the side cells. As thermal runaway propagated, the step time leading to the explosion was shortened. In addition, the number of cells simultaneously suffering thermal runaway radically increased as the fire propagated.

As shown in Figure 6b, the temperature gradient map of the LIB module was constructed when the abuse target cell reached the maximum temperature during the experiment. The maximum temperature of the center cell was ~1405 °C, while the average temperature of the side parts of the module was ~796 °C. These temperatures were sufficiently high to propagate the thermal runaway if there were other modules located beside it. In addition, a photograph of the entire exhausted module, caused by thermal runaway propagation, is shown in the figure.

Similarly, Figure 6c shows the temperatures and voltage of the BIF module with respect to time. The time taken to reach thermal runaway for the abused cell in the BIF module was similar to that of the LIB module at 396 s. However, the sudden temperature increase decreased by ~32% without the fire or explosions due to the direct FPM penetration into the abuse cell. Thereafter, the BIF module suffered thermal runaway once and only the venting gas was observed for the whole experiment.

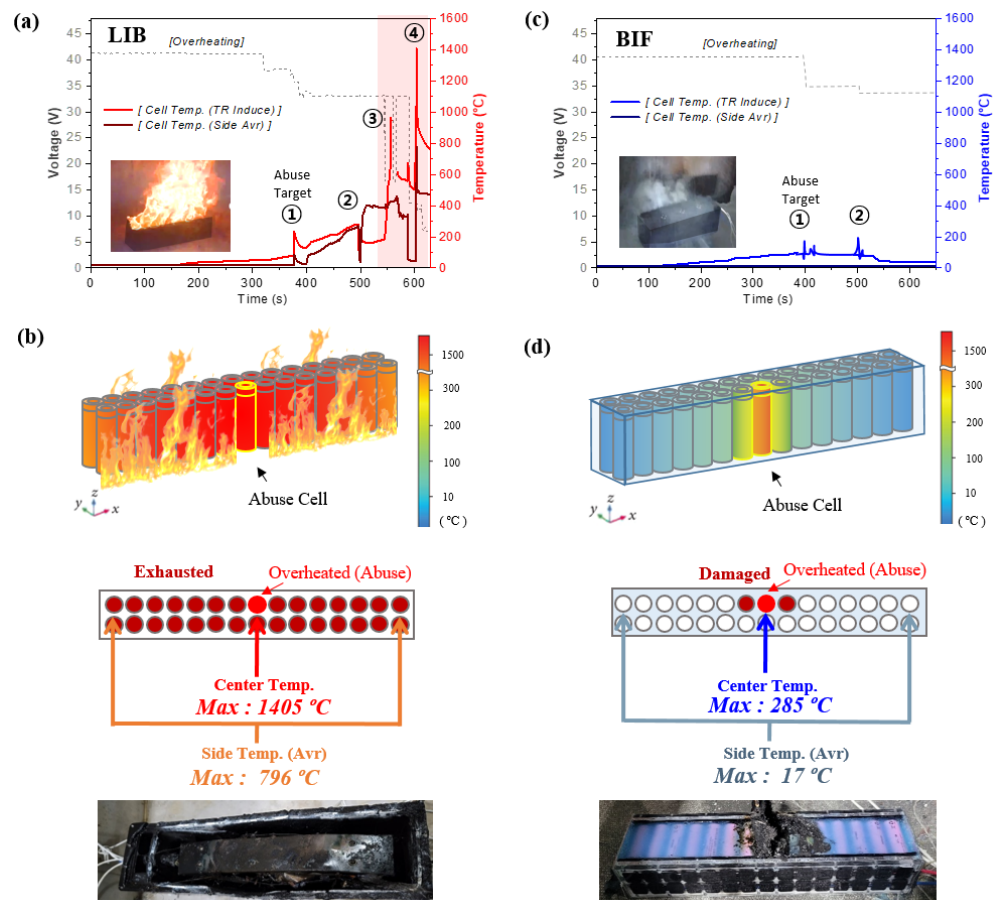


**Figure 6.** (a) Configuration of temperatures and voltage of the LIB module while abusing the target cell; (b) draft of the LIB module with an overheated single cell at the maximum temperature during the test, temperatures by location, and module after the test; (c) configuration of temperatures and voltages of the BIF module while abusing the target cell; (d) draft of the BIF module with an overheated single cell at the maximum temperature during the test, temperatures by location, and module after the test.

As shown in Figure 6d, the temperature gradient map of the BIF module was constructed when the abuse target cell reached the maximum temperature during the experiment. The maximum temperature of the center cell was  $\sim 285$  °C while that of the average temperature of the side part of the module was  $\sim 17$  °C. This temperature was sufficiently low to prevent thermal runaway propagation from the module in contact with the side. When one side of the BIF case module was opened after the test to determine the extent of the damage, only the batteries that were in direct contact with the abused cell suffered thermal runaway (1 ea) and slight damage (1 ea). Any other damages of the case or leakages did not occur.

### 3.3. Heat Management Efficiency during the Operation

High C-rate operation is required for applications, particularly in EVs, but the life cycle of LIB significantly decreases at high C-rates and temperatures [40–42]. Under extreme or harsh conditions in LIB applications, temperature measurements are used to determine the degree of heat management and estimate the available capacity (life) of the battery per cycle. Therefore, the heat management of batteries is important because the battery temperature during operation significantly impacts battery aging and performance [31,43,44], the fields where active research is being developed. As an example, the research of polydopamine regulation [45] or covalent organic framework with sulfonic acid groups [46] to Zn metal anode is currently being developed to solve this problem.

The high temperatures lead to a side reaction of SEI film formation with thickening, binder decomposition, and electrolyte decomposition [31,43,44]. These affect several degradation modes such as a loss of lithium-ion inventory, anode/cathode active material, electrolyte, and resistance increase. Then, these finally affect capacity and power fade [31,43,44]. The detailed experiments with this are held in the capacity fading and EIS test as follows.

The thermocouple was attached to the center of the cell body to record the temperature while charging and discharging the battery. Consequently, the surface temperature of the LIB cell increased significantly, and life expectancy decreased dramatically as the cycle progressed. In the BIF cell, the surface temperature was maintained and exhibited only slight degradation during long-term operation. The electrochemical performance of the BIF cell was improved through the heat management effect, owing to the heat absorption of the FPM.

Figure 7a shows the temperature changes in the LIB cell and BIF cell by cycle at a 40.0 °C 3C-rate discharge. Under the same conditions, the surface temperature of the LIB cell increased from 40.0 to 75.6 °C, while that of the BIF increased from 40.0 to 56.3 °C. Two main reasons exist for the temperature increase gap decreasing by ~2.2 times in the BIF cell. First, the increase in temperature decreased primarily because of the specific heat absorbance ability of the FPM. Second, the difference in capacity (heating reaction) time owing to thermal management reduces the temperature increase [47]. The maximum peak temperature was maintained as the cycles progressed.

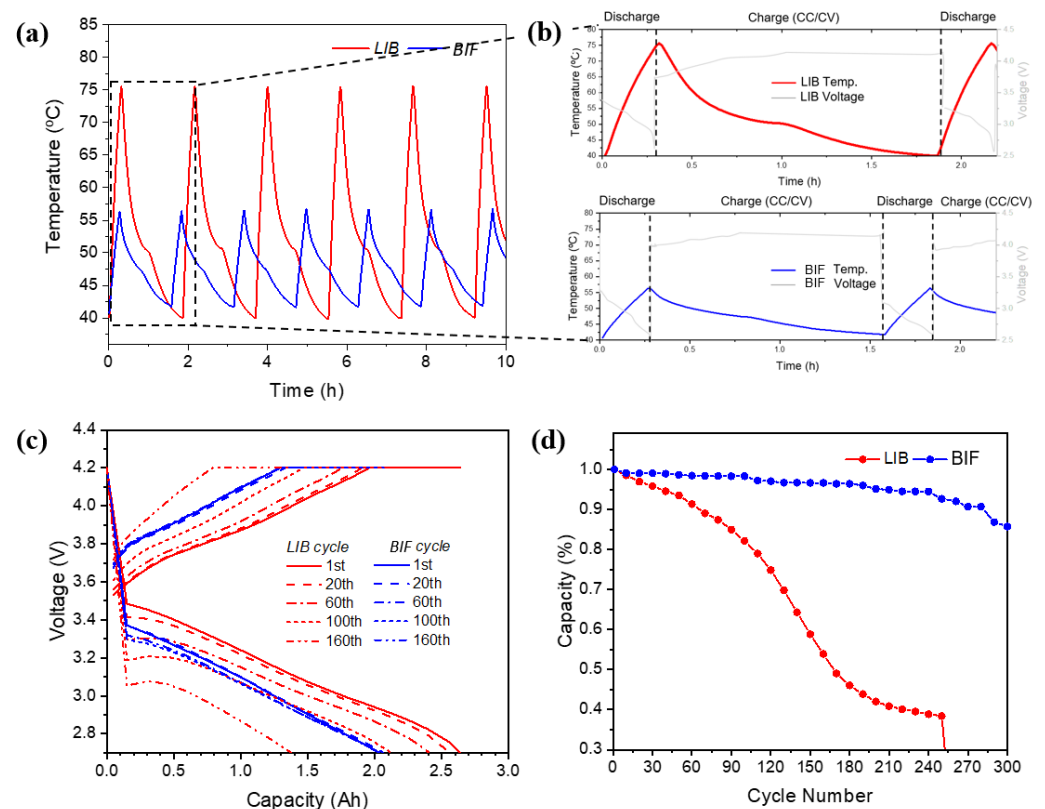


**Figure 7.** Heat management capability of BIF cell against LIB cell in harsh operating conditions (high C-rate and temperature): (a) temperature tendency of LIB cell and BIF cell by cycle, (b) enlargement, (c) charge and discharge voltage of the LIB cell and BIF cell, and (d) capacity comparison by cycle number.

Figure 7b shows the temperature changes in the LIB cell and BIF cell during cycling. During discharge, the exothermic reaction, activation polarization at the beginning, and concentration polarization at the end rapidly increased the current [48–51]. At this time, the impedance of the cell increased and decreased significantly in the constant-voltage charge

step compared to the constant-current charge. These factors account for the temperature variations [52].

Figure 7c compares the voltage of the LIB cell with that of the BIF cell based on the capacity. In LIB, as the cycle progresses, horizontal and vertical extrapolations occur quantitatively [31,53]. High currents lead to high overpotentials with increasing temperature. The capacity of the LIB cell was better than that of the BIF in the initial cycles owing to the high temperature. However, the capacity of the LIB cell becomes lower than that of the BIF cell after the 100th cycle. Additionally, fluctuations may occur in the early battery charging and discharging processes if the entropic heat negatively affects the driving conditions of certain batteries [31].

Figure 7d shows the capacity by number of cycles. The capacity of the LIB cell exhibited nonlinear aging [54] and rapidly decreased approximately after 100 cycles. This aging is caused by the degradation of internal battery components [32,55]. Battery capacity fading is caused by an increase in internal resistance as the material capacity decreases, such as the reaction between electrodes and electrolytes, reduction in active lithium ions, loss of electrons, and gas evolution [56,57]. This can be further accelerated at high temperatures [32]. Structural disorder, particle cracking, and the loss of electrical contact with the active materials may also be affected [56,57]. However, the BIF cell maintained its capacity as the cycle progressed due to thermal management, unlike the LIB cell.

An additional experiment in harsh conditions (low temperature) is referred to in Figure S4.

### 3.4. Electrochemical Impedance Spectroscopy (EIS) Comparison

Through impedance estimation, determining the degree of damage to each part or component of the battery in thermal management experiments is possible [58–64]. Electrochemical impedance spectroscopy was used to estimate the resistance by cycle [32,60,65,66]. Through this experiment, it is possible to know how much the thermal management effect of BIF prevents the aging of the components and increases its lifespan during the charge and discharge cycle.

A normal LIB EIS in a Nyquist plot is usually composed of the bulk resistance of the cell ( $R_b$ ), such as electrolytes, separators, or electrodes; the resistance and capacitance of the interfacial layer (RSEI/CPESEI); kinetics; charge-transfer resistance; double-layer capacitance ( $R_{ct}$ /CPEct); and diffusional effects of the lithium-ion on the host material ( $W$ ). The nickel–cobalt–aluminum (NCA) battery used in this cell has the advantages of high capacity and disadvantages such as structural and thermal stability, low inverse resistance to charge transfer, a short life cycle, and low resistance to microcracking [67–69] in the second semicircle ( $R_{ct}$ : charge transfer resistance).

As shown in Figure 8a, the LIB cell ceased operating after 45 cycles. In the BIF cell, the increased range of the second semicircle decreased considerably and operated for more than 84 cycles, as shown in Figure 8b. These ranges were compared between the BIF cell and LIB cell at a frequency of 0.147 Hz. The estimated values are provided in Table 4; in Cycle 42, the increased range of the second semicircle decreased in BIF by ~3.84 times [70–72]. Additionally, the cycle life of the battery increased by more than two times in the BIF compared with that in the LIB.

The detailed mechanisms of how the battery in the tests suffered damages are summarized in Figure S5 and detailed explanations are as follows through EIS results.

Because of the short operation time, aging caused by heat is difficult to detect, which prevents side reactions caused by electrolyte decomposition and decreases ion conductivity [32,53]. In addition, the temperature was well controlled in this experiment to limit exterior conditions. This resulted in bulk resistance ( $R_b$ ) remaining constant in both the LIB cell and BIF cell.

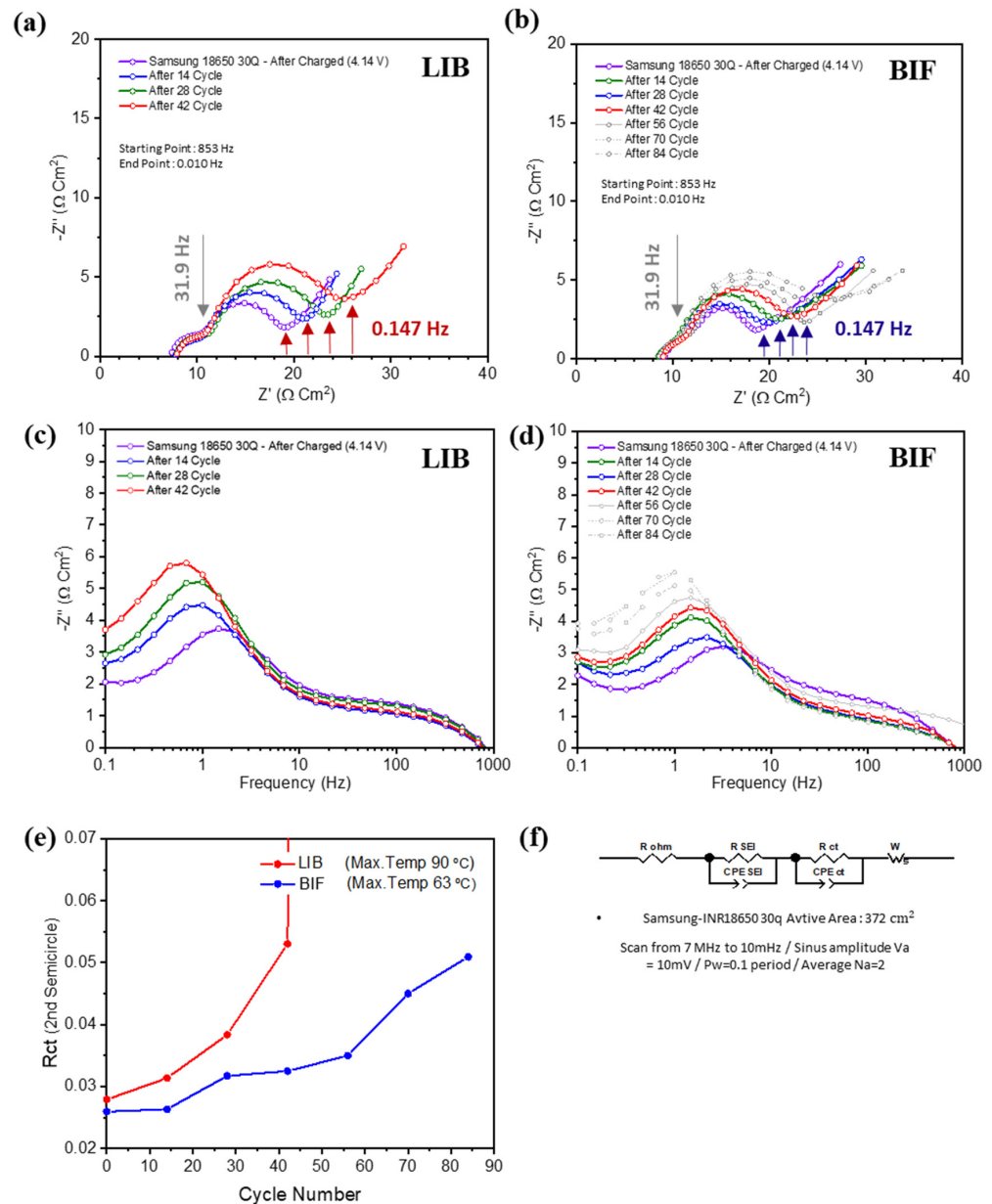


**Figure 8.** (a,b) Electrochemical impedance spectroscopy (EIS) comparison of LIB cell and BIF cell by cycle in Nyquist plot. (c,d) EIS comparison of LIB cell and BIF cell by cycle in Bodet plot. (e) Rct (2nd semicircle) impedance fitting data of LIB cell and BIF cell by the cycle number. (f) Equivalent circuit of battery for data fitting, active area of battery, and impedance measuring conditions.

**Table 4.** Increases in Rct (2nd Semicircle) impedance of LIB cell and BIF cell by cycle.

Rct (2nd Semicircle)	0 Cycles	14 Cycles	28 Cycles	42 Cycles
LIB ( $\Omega$ )	0.02791	0.03138	0.03838	0.05305
BIF ( $\Omega$ )	0.02597	0.02634	0.03174	0.03250

The capacity of the NCA battery decreased before double-layer formation; thus, the differences in the first semicircle (RSEI: interfacial resistance) caused by electrolyte decomposition were not large [56,73]. Generally, based on the Arrhenius equation, the charge transfer resistance decreases as the temperature increases. However, the maximum temperature of the LIB in this experiment was  $\sim 90^\circ\text{C}$ , and a reaction of the electrolyte with Li, decomposition, and gas evolution occurred. This high temperature and C-rate led to a

capacity decrease with aging from ~2805 to 2546 mAh [57]. These factors likely increase the second semicircle ( $R_{ct}$ : charge-transfer resistance) [67,74].

In the LIB, the cell operation ceased even though the maximum temperature was 90 °C (Internal Battery Protective device, PTC operating temperature was ~100 °C). Electrolyte decomposition may have caused the protection device to operate because of continuous gas or byproduct generation. Therefore, as the cycle progressed, the impedance of the LIB increased substantially. The CID, built inside the 18650, can be operated at a pressure approximately twice or lower than that of the top vent (1 MPa compared to 2.58 MPa) to detach the cathode contact and stop cell operation (XCT of the LIB was measured in the 3C/1C test, as shown in Figure S10) [18].

In summary, high temperature and current led to a Li reaction in the electrolyte, and dissolution led to gas evolution. This led to structural disordering and capacity fading but not to side reactions such as SEI layer formation and electrode oxidation.

As shown in Figure 8c,d, the Bodet graph was used to plot concentration changes with frequency. In the Bodet graph, a peak shift occurred at a low frequency (approximately 1 Hz, mass transport) during cycling. When mass transport or conductivity is low, the peak generally shifts to the left and upward. In the BIF cell, the increased range of the peak shift was approximately twice as small as that in the LIB cell.

The data were applied in Z-view, the impedance fitting program, using an equivalent equation model and circuit equations; the resulting graph is shown in Figure 8e. The life cycle of the BIF cell was two times better, with a slope three times lower than that of the LIB cell, which had a logarithmic shape [60]. Even though the expressed capacity of the BIF cell was lower than that of the LIB (2.5 Ah compared to approximately 2.8 Ah, ~86%) cell, the capacity retention rate was ~1.4 times higher [51].

Figure 8f represents the equivalent model used for fitting the impedance data [75,76], the active area of the single cell used in the module and experiments, and experimental conditions for estimating the impedance [77].

### 3.5. High Current Performance Comparison Using Pulse Test

Available power and resistance measurements under extreme operating conditions are important for LIB applications [5,42]. The C-rate, in particular, determines the performance [48]. Therefore, charging and discharging pulses have been applied to both LIB cells and BIF cells for a short period [78]. Under the pulse condition described in Figure 9a, the pulse capacity was 2.5 Ah. To maximize the effects of the discharge reaction, which is an exothermic reaction, the cell temperature was increased, the discharge C-rate was increased gradually from 1C to 6C, and the charge current was fixed at 0.5 C. The voltage and cell temperature were measured, and two cycles occurred at each C-rate for both LIB cells and BIF cells.

In the pulse test, the resistance (ohmic and non-ohmic) and high-power stability of the cell were used as the outputs. In addition, voltage and temperature were measured hourly at 40 °C for extreme environmental high-power verification [31,32].

As shown in Figure 9a,b, the surface temperature of the LIB cell increased considerably, whereas that of the BIF cell was low. As the discharge C-rate gradually elevated, the temperature gap between the battery cell and the case increased, and the maximum temperature gap between the LIB cell and BIF cell also increased. According to Table 5, the maximum C-rate achieved with the BIF was ~6, whereas that of the LIB was ~4. The maximum temperature of the BIF was ~87 °C at 6C, while that of the LIB was ~105 °C at 5C, which ceased the battery operation [48]. At a C-rate of 4C or less, the voltage change (resistance) of the BIF cell was greater than that of the LIB cell, indicating that the voltage efficiency was lower than LIB. This is because the high temperature of the LIB prevented a voltage drop.

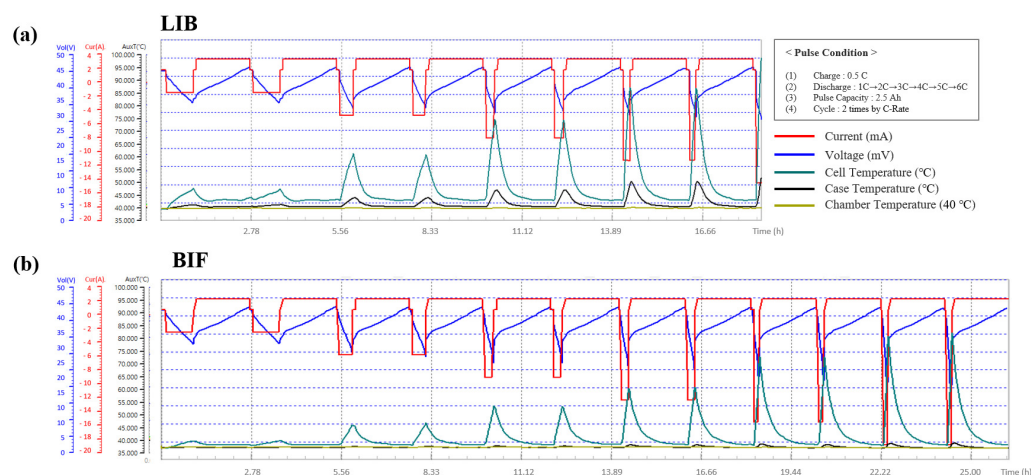


**Figure 9.** Performance (voltage efficiency, temperature) comparisons by gradual discharge C-rate increases in (a) LIB cells and (b) BIF cells using pulse test.

**Table 5.** Maximum Temperatures (End of Discharge in each Cycle) of LIB Cells and BIF Cells in Pulse Test.

Temperature (°C)	1C		2C		3C		4C		5C		6C	
LIB Cell	47.2	47.7	61.4	61.9	75.6	75.8	90.9	91.1	105.1	-	-	-
LIB Case	41.6	41.7	44.2	44.3	47.9	47.9	50.8	50.9	52.6	-	-	-
BIF Cell	42.5	42.6	49.1	49.2	57.3	57.4	65.3	65.4	77.6	77.7	87.8	87.9
BIF Case	40.3	40.3	40.5	40.5	40.9	40.9	41.3	41.4	41.8	41.8	42.1	42.2

This allowed the LIB to easily reach 100 °C, the temperature where protection devices such as PTCs operate, as shown in Figure S10. This prevents the battery from leading to thermal runaway by stopping the battery operation.

Through thermal management, the operating current range of the BIF cell was increased. Therefore, operation over a wide current range was made possible.

Additional detailed information such as voltage differences and resistances at each C-rate is described in Figures S6 and S7.

### 3.6. Module Temperature by Spots

In multiple cell arrays, such as battery modules or packs, the internal status of the cell, including its capacity, resistance, state of charge, and health, may differ in each cell [79]. Additionally, exterior effects, such as varied temperature and contact resistance, affect the current deviation and decrease the battery performance [7,80]. The temperatures and voltage profile of the BIF module during normal operations are shown in Figures S8 and S9. The performance of the modules gradually decreases as the cycle progresses, owing to cell deviations [81]. These phenomena in cell arrays are called imbalances (or unbalancing).

The imbalance increases when the temperatures of the cells comprising the battery in the module are different [55,82]. Figure 10a shows the maximum temperature of the LIB module while cycling the battery at a 0.5 C-rate. Fifteen spots (the center of the cell body in each spot) of the module were measured during operation. This configuration shows the temperature-fitting diagram of the LIB module at the same time as that of the BIF module. The temperature significantly increased at the center of the module, whereas that at the side was low [67,83]. Figure 10b shows the same experiment performed in the BIF module. Because the temperature increase range was smaller than that of the LIB module through thermal management, the thermal deviation between the cells was minor.

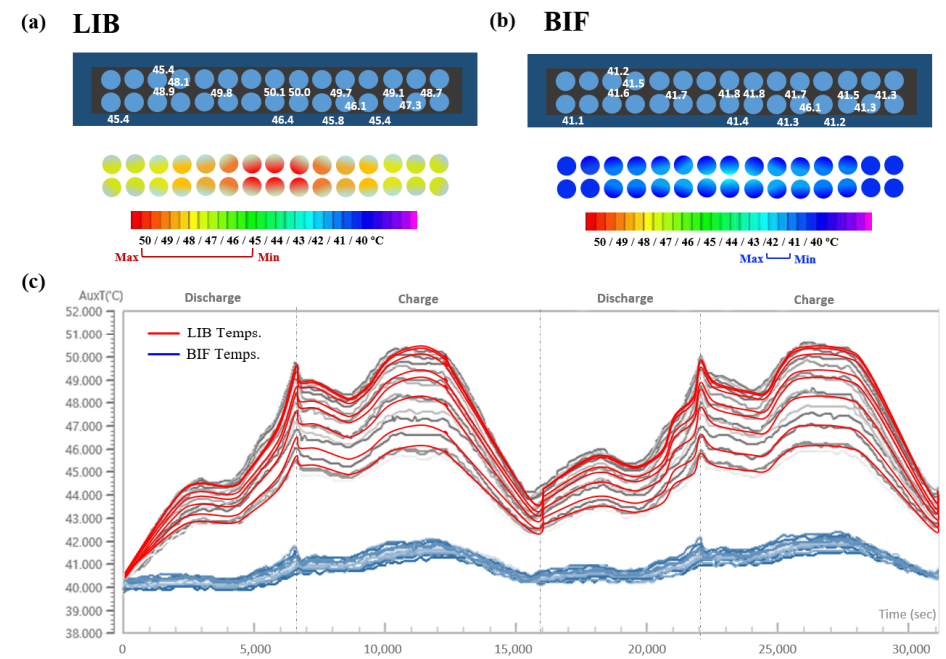


**Figure 10.** Temperature of the module by spots and their configuration while cycling; (a) LIB module, (b) BIF module, (c) and temperature comparisons of the module by time and spots, grey lines indicate charge and discharge cycle.

Figure 10c shows the temperature of the LIB and BIF modules by spot during the cycle at 40 °C. In the BIF modules, both the maximum and cell temperature deviations decreased, and the gap between the maximum and minimum cell temperatures was smaller than that in the LIB module. The maximum cell temperature of the LIB module was  $\sim 50.1$  °C, whereas the minimum cell temperature at the same time was  $\sim 45.4$  °C. The temperature gap was  $\sim 4.7$  °C. Concurrently, the maximum cell temperature of the BIF module was  $\sim 41.2$  °C, and the minimum cell temperature was  $\sim 40.5$  °C. In the BIF module, the temperature gap was  $\sim 0.7$  °C, 2.8 times smaller than that of the LIB module.

### 3.7. Module in Application (Kickboard)

As shown in Figure 11a, an electric kickboard was used to realize the performance of the BIF in the module, which was compared to that of the LIB module. The model of the kickboard was a Red Wing Black by Autech.

Figure 11b illustrates the five spots of the thermocouples attached to both the LIB and BIF modules. Owing to the structure of the LIB module, temperature-sensing lines were attached to the surface of the module.

Figure 11c shows the temperatures of the LIB and BIF modules by spot during the kickboard operation. The temperature of the module was  $\sim 21$  °C right before operation. The kickboard was operated continuously at 1.55C (maximum C-rate) for 30 min. During operation, the temperatures of the LIB and BIF modules increase [84]. However, the temperature of the LIB module varied substantially by spot, whereas that of the BIF module exhibited only minor differences. The maximum temperature of the LIB was  $\sim 24.8$  °C, while the lowest cell temperature at that time was  $\sim 23.2$  °C. In the BIF module, the maximum temperature of the cell was  $\sim 21.5$  °C, while the lowest was 21.2 °C. As a result of the module cycle, not only did the BIF prevent a module temperature increase but it also lowered the temperature gaps of the cells through thermal management.

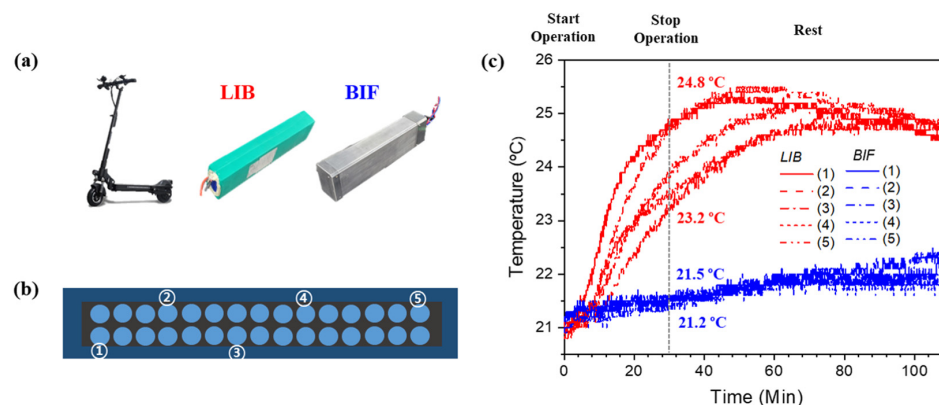


**Figure 11.** (a) Setup configuration of e-kickboard with LIB and BIF modules; (b) temperature measuring spots of the module; (c) temperature of LIB and BIF module by spots during kickboard operation and rest.

That being said, after the operation, the temperature of the LIB module in the kickboard continued to increase for ~30 min. Although it was not operating, the power of the BMS, residual heat, closed structure, and exterior environment were affected by the increment of the temperature. Thereafter, the temperature of the entire cell in the LIB began to decrease smoothly, and the temperature gap between the cells decreased. However, the temperature did not return to the initial value. The mobility applications that utilize batteries often require high power (more than a C-rate of 4) in extreme conditions. If the module was operated at a high C-rate, the continuous cycle of this operation may have overheated the battery module during real operation, which significantly affected the electrochemical performances and safety.

The temperature of the BIF module also increased after operation for the same reason as that for the LIB. However, the slope of the temperature increase significantly decreased compared to that of the LIB module, owing to the large heat capacity of the FPM. The temperature of the module began to decrease later than that of the LIB module. The temperature continued to increase at a few points of the BIF module, whereas at others it started to decrease. These improve the capacity and safety of the battery.

#### 4. Conclusions

This study proposes a BIF as a solution to address battery fire risks while facilitating effective heat management. The BIF cell and module were developed and thoroughly investigated, including its components, construction, and potential applications.

Notably, the BIF module effectively mitigated the size of explosions and fire occurrences by impeding the propagation of thermal runaway. This is because the FPM in direct contact with the battery, by immersion structure, can immediately penetrate into the battery when thermal runaway occurs. With significantly lower temperatures observed in the side sections of the cells during such an experiment, it is anticipated that large-scale battery applications such as ESSs will face minimal risks of fire or exhaustion.

Simultaneously, the BIF module enables superior thermal management compared with the LIB module, particularly in extreme environments at all times. This feature enhances battery life and reduces the thermal deviation between cells caused by high currents. In addition, it has the advantages of reducing maintenance costs and being eco-friendly compared to air conditioners that consume power and emit greenhouse gases.

Although further numerical comparisons with other systems are needed, performance efficiencies of the BIF are expected to be high due to the superior agent and immersion structure. These exceed the battery cooling parameters, such as heat capacity, conductance, reaction speed of the agent, and its effecting area on the battery.

This study lays the foundation for future investigations of BIF and their integration into practical battery systems. Further studies are warranted to advance the commercialization of BIF.

First, research on the functional components of BIF, particularly FPM, should be conducted. Establishing the precise mechanisms through which FPM suffocates fires and diminishes heat is essential. Furthermore, improvements in the FPM composition should be pursued to enhance thermal management capabilities, including heat conductivity and capacity, thereby optimizing the performance of the BIF.

Second, in-depth research is required on sealing layers that block FPM penetration completely. Developing a structural design with a thin sealing layer in the form of housing that surrounds the FPM can not only enhance the fire suppression performance but also provide a favorable structure for battery insertion.

Third, the efforts must be directed towards addressing the challenges associated with energy density reduction in BIF. The incorporation of functional elements leads to a reduction in energy density compared with conventional LIBs. Thus, strategies to minimize the amount of FPM while considering thermal management, fire suppression, and specific application requirements should be explored. This necessitates research in areas such as thermodynamics, electrochemistry, simulation techniques [85], and three-dimensional heat flow equations over time and dimensions, as well as the consideration of different LIB cell types (cylindrical, prismatic, or pouch) and their arrangements within the module [86].

Finally, experimental methodologies should be developed to estimate the real battery applications on a larger scale, such as ESSs. This would involve investigating operational methods and conditions such as the presence of a BMS, module stacking configurations, applied applications, and the flow of FPMs. If the BIF is successfully applied to ESSs, it is expected to increase the battery charging rate by replacing fire extinguishing facilities, simplifying cooling systems, and securing stability.

By improving these research areas, the potential of BIF as an advanced battery technology can be realized.

**Supplementary Materials:** The following supporting information can be downloaded at: <https://www.mdpi.com/article/10.3390/en17102418/s1>, Figure S1: (a) Fire Suppression Process of the FPM when thermal runaway happens in battery (b) Flame emission Test on a normal paper sheet and the sheet with the FPM (c) Fire suppression test by injection of water and the FPM; Figure S2: Maximum energy generated by LIB short circuit, and the heat absorbance performance of BIF when theoretical amount of the FPM is applied to the cell (3.7 V/50 mAh/LCO Pouch cell); Figure S3: Exothermic chain reactions of LIB by thermal runaway stages; Figure S4: Capacity by cycle and voltage efficiency comparison between LIB and BIF at low temperature (5 °C); Figure S5: Influencing factors and degradation mechanisms of BIF during cycling; Figure S6: Delta V comparisons with gradual C-rate increases for LIB and BIF; Figure S7: Resistance comparisons by gradual C-rate increases of LIB and BIF; Figure S8: Temperature measuring spots and temperatures of BIF module during cycling; Figure S9: Electrochemical performances and temperatures of BIF module during cycling; Figure S10: XCT data of the cylindrical cell before and after the operation; Table S1: Material properties comparison table for the agent used for battery fire. References [18,31,32,53,58,66,77,79,83,87,88] are cited in Supplementary File.

**Author Contributions:** Conceptualization, Y.C.; methodology, J.B.; validation, Y.K.; formal analysis, J.B.; investigation, J.B.; resources, Y.K.; data curation, J.B.; writing—original draft preparation, J.B.; writing—review and editing, J.B.; visualization, J.B.; supervision, Y.K.; project administration, Y.K.; funding acquisition, Y.K. All authors have read and agreed to the published version of the manuscript.

**Funding:** This work (study) was supported by the Korea Institute of Energy Technology Evaluation and Planning (KETEP) grant funded by the MOTIE (20215610100040, Development of 20 Wh seawater secondary battery unit cell) and the Korea Research Institute for Defense Technology planning and advancement (KRIT) grant funded by the Korean government (DAPA (Defense Acquisition Program Administration)) (No. 21-107-D00-009, Design and development of core materials and single cells for seawater secondary batteries, 2024).

**Data Availability Statement:** All authors of articles published in MDPI journals can share their research data with the authors' agreement.

**Conflicts of Interest:** Author Youngsik Kim was employed by the 4TOONE Corporation. The remaining authors declare that the research was conducted in the absence of any commercial or financial relationships that could be construed as a potential conflict of interest.

## References

1. Hameer, S.; van Niekerk, J.L. A review of large-scale electrical energy storage. *Int. J. Energy Res.* **2015**, *39*, 1179–1195. [[CrossRef](#)]
2. Li, Y.; Zhou, Z.; Hu, L.; Bai, M.; Gao, L.; Li, Y.; Liu, X.; Li, Y.; Song, Y. Experimental studies of liquid immersion cooling for 18650 lithium-ion battery under different discharging conditions. *Case Stud. Therm. Eng.* **2022**, *34*, 102034. [[CrossRef](#)]
3. Wang, Q.; Jiang, B.; Li, B.; Yan, Y. A critical review of thermal management models and solutions of lithium-ion batteries for the development of pure electric vehicles. *Renew. Sustain. Energy Rev.* **2016**, *64*, 106–128. [[CrossRef](#)]
4. Feng, X.; Ren, D.; He, X.; Ouyang, M. Mitigating thermal runaway of lithium-ion batteries. *Joule* **2020**, *4*, 743–770. [[CrossRef](#)]
5. Chen, Y.; Kang, Y.; Zhao, Y.; Wang, L.; Liu, J.; Li, Y.; Liang, Z.; He, X.; Li, X.; Tavajohi, N.; et al. A review of lithium-ion battery safety concerns: The issues, strategies, and testing standards. *J. Energy Chem.* **2021**, *59*, 83–99. [[CrossRef](#)]
6. Yuan, S.; Chang, C.; Yan, S.; Zhou, P.; Qian, X.; Yuan, M.; Liu, K. A review of fire-extinguishing agent on suppressing lithium-ion batteries fire. *J. Energy Chem.* **2021**, *62*, 262–280. [[CrossRef](#)]
7. Diaz, L.B.; He, X.; Hu, Z.; Restuccia, F.; Marinescu, M.; Barreras, J.V.; Patel, V.; Offer, G.; Rein, G. Meta-review of fire safety of lithium-ion batteries: Industry challenges and research contributions. *J. Electrochem. Soc.* **2020**, *167*, 090559. [[CrossRef](#)]
8. Wang, Q.; Shao, G.; Duan, Q.; Chen, M.; Li, Y.; Wu, K.; Liu, B.; Peng, P.; Sun, J. The efficiency of heptafluoropropane fire extinguishing agent on suppressing the lithium titanate battery fire. *Fire Technol.* **2016**, *52*, 387–396. [[CrossRef](#)]
9. Zhang, L.; Li, Y.; Duan, Q.; Chen, M.; Xu, J.; Zhao, C.; Sun, J.; Wang, Q. Experimental study on the synergistic effect of gas extinguishing agents and water mist on suppressing lithium-ion battery fires. *J. Energy Storage* **2020**, *32*, 101801. [[CrossRef](#)]
10. Xu, J.; Guo, P.; Duan, Q.; Yu, X.; Zhang, L.; Liu, Y.; Wang, Q. Experimental study of the effectiveness of three kinds of extinguishing agents on suppressing lithium-ion battery fires. *Appl. Therm. Eng.* **2020**, *171*, 115076. [[CrossRef](#)]
11. Yang, X.; Duan, Y.; Zhang, Z.; Feng, X.; Chen, T.; Xu, C.; Rui, X.; Ouyang, M.; Lu, L.; Han, X.; et al. An experimental study on preventing thermal runaway propagation in lithium-ion battery module using aerogel and liquid cooling plate together. *Fire Technol.* **2020**, *56*, 2579–2602. [[CrossRef](#)]
12. Liu, Y.; Duan, Q.; Li, K.; Chen, H.; Wang, Q. Experimental study on fire extinguishing of large-capacity lithium-ion batteries by various fire extinguishing agents. *Energy Storage Sci. Technol.* **2018**, *7*, 1105.
13. Han, X.; Lu, L.; Zheng, Y.; Feng, X.; Li, Z.; Li, J.; Ouyang, M. A review on the key issues of the lithium ion battery degradation among the whole life cycle. *eTransportation* **2019**, *1*, 100005. [[CrossRef](#)]
14. Zhang, L.; Jin, K.; Sun, J.; Wang, Q. A Review of Fire-Extinguishing Agents and Fire Suppression Strategies for Lithium-Ion Batteries Fire. *Fire Technol.* **2022**, 1–42. [[CrossRef](#)]
15. Said, A.O.; Stoliarov, S.I. Analysis of effectiveness of suppression of lithium ion battery fires with a clean agent. *Fire Saf. J.* **2021**, *121*, 103296. [[CrossRef](#)]
16. Huang, Z.; Liu, P.; Duan, Q.; Zhao, C.; Wang, Q. Experimental investigation on the cooling and suppression effects of liquid nitrogen on the thermal runaway of lithium ion battery. *J. Power Sources* **2021**, *495*, 229795. [[CrossRef](#)]
17. Kuznetsov, G.; Kopylov, N.; Sushkina, E.; Zhdanova, A. Adaptation of fire-fighting systems to localization of fires in the premises. *Energies* **2022**, *15*, 522. [[CrossRef](#)]
18. Xu, B.; Kong, L.; Wen, G.; Pecht, M.G. Protection devices in commercial 18650 lithium-ion batteries. *IEEE Access* **2021**, *9*, 66687–66695. [[CrossRef](#)]
19. Sabbah, R.; Kizilel, R.; Selman, J.R.; Al-Hallaj, S. Active (air-cooled) vs. passive (phase change material) thermal management of high power lithium-ion packs: Limitation of temperature rise and uniformity of temperature distribution. *J. Power Sources* **2008**, *182*, 630–638. [[CrossRef](#)]
20. Lan, C.; Xu, J.; Qiao, Y.; Ma, Y. Thermal management for high power lithium-ion battery by minichannel aluminum tubes. *Appl. Therm. Eng.* **2016**, *101*, 284–292. [[CrossRef](#)]
21. Niu, H.; Chen, C.; Liu, Y.; Li, L.; Li, Z.; Ji, D.; Huang, X. Mitigating thermal runaway propagation of NCM 811 prismatic batteries via hollow glass microspheres plates. *Process Saf. Environ. Prot.* **2022**, *162*, 672–683. [[CrossRef](#)]
22. Weng, J.; Ouyang, D.; Yang, X.; Chen, M.; Zhang, G.; Wang, J. Alleviation of thermal runaway propagation in thermal management modules using aerogel felt coupled with flame-retarded phase change material. *Energy Conv. Manag.* **2019**, *200*, 112071. [[CrossRef](#)]
23. Li, L.; Xu, C.; Chang, R.; Yang, C.; Jia, C.; Wang, L.; Song, J.; Li, Z.; Zhang, F.; Fang, B.; et al. Thermal-responsive, super-strong, ultrathin firewalls for quenching thermal runaway in high-energy battery modules. *Energy Storage Mater.* **2021**, *40*, 329–336. [[CrossRef](#)]
24. Lin, S.; Ling, Z.; Li, S.; Cai, C.; Zhang, Z.; Fang, X. Mitigation of lithium-ion battery thermal runaway and inhibition of thermal runaway propagation using inorganic salt hydrate with integrated latent heat and thermochemical storage. *Energy* **2023**, *266*, 126481. [[CrossRef](#)]

25. Ahmadi, L.; Young, S.B.; Fowler, M.; Fraser, R.A.; Achachlouei, M.A. A cascaded life cycle: Reuse of electric vehicle lithium-ion battery packs in energy storage systems. *Int. J. LCA* **2017**, *22*, 111–124. [[CrossRef](#)]
26. Bae, J.; Bae, H.; Cho, J.; Jung, J.; Choi, Y.; Kim, Y. Zero fire battery concept: Water-in-battery. *J. Mater. Chem. A* **2022**, *10*, 6481–6488. [[CrossRef](#)]
27. Chin, C.S.; Jia, J.; Chiew, J.H.K.; Da Toh, W.; Gao, Z.; Zhang, C.; McCann, J. System design of underwater battery power system for marine and offshore industry. *J. Energy Storage* **2019**, *21*, 724–740. [[CrossRef](#)]
28. Hoelle, S.; Scharner, S.; Asanin, S.; Hinrichsen, O. Analysis on thermal runaway behavior of prismatic Lithium-ion batteries with autoclave calorimetry. *J. Electrochem. Soc.* **2021**, *168*, 120515. [[CrossRef](#)]
29. Lamb, J.; Torres-Castro, L.; Hewson, J.C.; Shurtz, R.C.; Preger, Y. Investigating the role of energy density in thermal runaway of lithium-ion batteries with accelerating rate calorimetry. *J. Electrochem. Soc.* **2021**, *168*, 060516. [[CrossRef](#)]
30. Chen, M.; Sun, Q.; Li, Y.; Wu, K.; Liu, B.; Peng, P.; Wang, Q. A thermal runaway simulation on a lithium titanate battery and the battery module. *Energies* **2015**, *8*, 490–500. [[CrossRef](#)]
31. Wang, K.; Gao, F.; Zhu, Y.; Liu, H.; Qi, C.; Yang, K.; Jiao, Q. Internal resistance and heat generation of soft package  $\text{Li}_4\text{Ti}_5\text{O}_{12}$  battery during charge and discharge. *Energy* **2018**, *149*, 364–374. [[CrossRef](#)]
32. Zhang, X.; Li, Z.; Luo, L.; Fan, Y.; Du, Z. A review on thermal management of lithium-ion batteries for electric vehicles. *Energy* **2022**, *238*, 121652. [[CrossRef](#)]
33. Kong, D.; Peng, R.; Ping, P.; Du, J.; Chen, G.; Wen, J. A novel battery thermal management system coupling with PCM and optimized controllable liquid cooling for different ambient temperatures. *Energy Convers. Manag.* **2020**, *204*, 112280. [[CrossRef](#)]
34. Liu, T.; Tao, C.; Wang, X. Cooling control effect of water mist on thermal runaway propagation in lithium ion battery modules. *Appl. Energy* **2020**, *267*, 115087. [[CrossRef](#)]
35. Liu, T.; Hu, J.; Zhu, X.; Wang, X. A practical method of developing cooling control strategy for thermal runaway propagation prevention in lithium ion battery modules. *J. Energy Storage* **2022**, *50*, 104564. [[CrossRef](#)]
36. Liu, T.; Liu, Y.; Wang, X.; Kong, X.; Li, G. Cooling control of thermally-induced thermal runaway in 18,650 lithium ion battery with water mist. *Energy Conv. Manag.* **2019**, *199*, 111969. [[CrossRef](#)]
37. Huang, Z.; Liu, J.; Zhai, H.; Wang, Q. Experimental investigation on the characteristics of thermal runaway and its propagation of large-format lithium ion batteries under overcharging and overheating conditions. *Energy* **2021**, *233*, 121103. [[CrossRef](#)]
38. Kim, S.K.; Choi, S.G.; Jin, S.Y.; Bang, S.S. An experimental study on fire risks due to overcharge and external heat of ESS lithium battery. *Fire Sci. Eng.* **2019**, *33*, 59–69. [[CrossRef](#)]
39. Wang, H.; Shi, W.; Hu, F.; Wang, Y.; Hu, X.; Li, H. Over-heating triggered thermal runaway behavior for lithium-ion battery with high nickel content in positive electrode. *Energy* **2021**, *224*, 120072. [[CrossRef](#)]
40. Ramadass, P.; Haran, B.; White, R.; Popov, B.N. Capacity fade of Sony 18650 cells cycled at elevated temperatures: Part I. Cycling performance. *J. Power Sources* **2002**, *112*, 606–613. [[CrossRef](#)]
41. Liao, L.; Zuo, P.; Ma, Y.; Chen, X.; An, Y.; Gao, Y.; Yin, G. Effects of temperature on charge/discharge behaviors of  $\text{LiFePO}_4$  cathode for Li-ion batteries. *Electrochim. Acta* **2012**, *60*, 269–273. [[CrossRef](#)]
42. Rezvanianiani, S.M.; Liu, Z.; Chen, Y.; Lee, J. Review and recent advances in battery health monitoring and prognostics technologies for electric vehicle (EV) safety and mobility. *J. Power Sources* **2014**, *256*, 110–124. [[CrossRef](#)]
43. Monika, K.; Chakraborty, C.; Roy, S.; Sujith, R.; Datta, S.P. A numerical analysis on multi-stage Tesla valve based cold plate for cooling of pouch type Li-ion batteries. *Int. J. Heat Mass Transf.* **2021**, *177*, 121560. [[CrossRef](#)]
44. Yang, S.; Ling, C.; Fan, Y.; Yang, Y.; Tan, X.; Dong, H. A review of lithium-ion battery thermal management system strategies and the evaluate criteria. *Int. J. Electrochem. Sci.* **2019**, *14*, 6077–6107. [[CrossRef](#)]
45. Wang, T.; Wang, P.; Pan, L.; He, Z.; Dai, L.; Wang, L.; Liu, S.; Jun, S.C.; Lu, B.; Liang, S.; et al. Stabling zinc metal anode with polydopamine regulation through dual effects of fast desolvation and ion confinement. *Adv. Energy Mater.* **2023**, *13.5*, 2203523. [[CrossRef](#)]
46. Li, B.; Ruan, P.; Xu, X.; He, Z.; Zhu, X.; Pan, L.; Peng, Z.; Liu, Y.; Zhou, P.; Lu, B.; et al. Covalent Organic Framework with 3D Ordered Channel and Multi-Functional Groups Endows Zn Anode with Superior Stability. *Nano-Micro Lett.* **2024**, *16*, 76. [[CrossRef](#)]
47. Abe, Y.; Hori, N.; Kumagai, S. Electrochemical impedance spectroscopy on the performance degradation of  $\text{LiFePO}_4$ /graphite lithium-ion battery due to charge-discharge cycling under different C-rates. *Energies* **2019**, *12*, 4507. [[CrossRef](#)]
48. Heubner, C.; Schneider, M.; Lämmel, C.; Michaelis, A. Local heat generation in a single stack lithium ion battery cell. *Electrochim. Acta* **2015**, *186*, 404–412. [[CrossRef](#)]
49. Fly, A.; Chen, R. Rate dependency of incremental capacity analysis (dQ/dV) as a diagnostic tool for lithium-ion batteries. *J. Energy Storage* **2020**, *29*, 101329. [[CrossRef](#)]
50. Dubarry, M.; Truchot, C.; Liaw, B.Y.; Gering, K.; Sazhin, S.; Jamison, D.; Michelbacher, C. Evaluation of commercial lithium-ion cells based on composite positive electrode for plug-in hybrid electric vehicle applications: III. Effect of thermal excursions without prolonged thermal aging. *J. Electrochem. Soc.* **2012**, *160*, A191. [[CrossRef](#)]
51. Zhang, P.; Yuan, T.; Pang, Y.; Peng, C.; Yang, J.; Ma, Z.F.; Zheng, S. Influence of current density on graphite anode failure in lithium-ion batteries. *J. Electrochem. Soc.* **2019**, *166*, A5489. [[CrossRef](#)]

52. Hernandez Lugo, D.; Clarke, S.; Miller, T.; Redifer, M.; Foster, T. X-57 Maxwell Battery from Cell Level to System Level Design and Testing (No. GRC-E-DAA-TN59208). 12 July 2018. Available online: <https://ntrs.nasa.gov/citations/20180005737> (accessed on 6 May 2024).
53. Kwon, S.J.; Lee, S.E.; Lim, J.H.; Choi, J.; Kim, J. Performance and life degradation characteristics analysis of NCM LIB for BESS. *Electronics* **2018**, *7*, 406. [[CrossRef](#)]
54. Rohr, S.; Müller, S.; Baumann, M.; Kerler, M.; Ebert, F.; Kaden, D.; Lienkamp, M. Quantifying uncertainties in reusing lithium-ion batteries from electric vehicles. *Procedia Manuf.* **2017**, *8*, 603–610. [[CrossRef](#)]
55. Capron, O.; Samba, A.; Omar, N.; Coosemans, T.; Van den Bossche, P.; Van Mierlo, J. Lithium-ion batteries: Thermal behaviour investigation of unbalanced modules. *Sustainability* **2015**, *7*, 8374–8398. [[CrossRef](#)]
56. Kabir, M.M.; Demirocak, D.E. Degradation mechanisms in Li-ion batteries: A state-of-the-art review. *Int. J. Energy Res.* **2017**, *41*, 1963–1986. [[CrossRef](#)]
57. Thompson, A.W. Economic implications of lithium ion battery degradation for Vehicle-to-Grid (V2X) services. *J. Power Sources* **2018**, *396*, 691–709. [[CrossRef](#)]
58. Momma, T.; Matsunaga, M.; Mukoyama, D.; Osaka, T. Ac impedance analysis of lithium ion battery under temperature control. *J. Power Sources* **2012**, *216*, 304–307. [[CrossRef](#)]
59. Zhou, X.; Huang, J.; Pan, Z.; Ouyang, M. Impedance characterization of lithium-ion batteries aging under high-temperature cycling: Importance of electrolyte-phase diffusion. *J. Power Sources* **2019**, *426*, 216–222. [[CrossRef](#)]
60. Choi, W.; Shin, H.C.; Kim, J.M.; Choi, J.Y.; Yoon, W.S. Modeling and applications of electrochemical impedance spectroscopy (EIS) for lithium-ion batteries. *J. Electrochem. Sci. Technol.* **2020**, *11*, 1–13. [[CrossRef](#)]
61. Vadha, P.; Hu, J.; Johnson, M.J.; Stocker, R.; Braglia, M.; Brett, D.J.; Rettie, A.J. Electrochemical impedance spectroscopy for all-solid-state batteries: Theory, methods and future outlook. *ChemElectroChem* **2021**, *8*, 1930–1947. [[CrossRef](#)]
62. Meddings, N.; Heinrich, M.; Overney, F.; Lee, J.-S.; Ruiz, V.; Napolitano, E.; Seitz, S.; Hinds, G.; Raccichini, R.; Gabers, M.; et al. Application of electrochemical impedance spectroscopy to commercial Li-ion cells: A review. *J. Power Sources* **2020**, *480*, 228742. [[CrossRef](#)]
63. Pastor-Fernández, C.; Widanage, W.D.; Marco, J.; Gama-Valdez, M.Á.; Chouchelamane, G.H. Identification and quantification of ageing mechanisms in Lithium-ion batteries using the EIS technique. In Proceedings of the 2016 IEEE Transportation Electrification Conference and Expo (ITEC), Dearborn, MI, USA, 27–29 June 2016; pp. 1–6.
64. Locorotondo, E.; Cultrera, V.; Pugi, L.; Berzi, L.; Pasquali, M.; Andrenacci, N.; Lutzemberger, G.; Pierini, M. Impedance spectroscopy characterization of lithium batteries with different ages in second life application. In Proceedings of the 2020 IEEE International Conference on Environment and Electrical Engineering and 2020 IEEE Industrial and Commercial Power Systems Europe (EEEIC/I&CPS Europe), Madrid, Spain, 9–12 June 2020; pp. 1–6.
65. Rad, M.S.; Danilov, D.L.; Baghalha, M.; Kazemeini, M.; Notten, P.H.L. Adaptive thermal modeling of Li-ion batteries. *Electrochim. Acta* **2013**, *102*, 183–195.
66. Zhu, J.G.; Sun, Z.C.; Wei, X.Z.; Dai, H.F. A new lithium-ion battery internal temperature on-line estimate method based on electrochemical impedance spectroscopy measurement. *J. Power Sources* **2015**, *274*, 990–1004. [[CrossRef](#)]
67. Corso, B.L.; Perez, I.; Sheps, T.; Sims, P.C.; Gül, O.T.; Collins, P.G. Electrochemical charge-transfer resistance in carbon nanotube composites. *Nano Lett.* **2014**, *14*, 1329–1336. [[CrossRef](#)]
68. Xia, H.; Liu, C.; Shen, L.; Yu, J.; Li, B.; Kang, F.; He, Y.B. Structure and thermal stability of  $\text{LiNi}_{0.8}\text{Co}_{0.15}\text{Al}_{0.05}\text{O}_2$  after long cycling at high temperature. *J. Power Sources* **2020**, *450*, 227695. [[CrossRef](#)]
69. Diaz, F.; Wang, Y.; Moorthy, T.; Friedrich, B. Degradation mechanism of nickel-cobalt-aluminum (NCA) cathode material from spent lithium-ion batteries in microwave-assisted pyrolysis. *Metals* **2018**, *8*, 565. [[CrossRef](#)]
70. Andre, D.; Meiler, M.; Steiner, K.; Wimmer, C.; Soczka-Guth, T.; Sauer, D.U. Characterization of high-power lithium-ion batteries by electrochemical impedance spectroscopy. I. Experimental investigation. *J. Power Sources* **2011**, *196*, 5334–5341. [[CrossRef](#)]
71. Gaberšček, M. Understanding Li-based battery materials via electrochemical impedance spectroscopy. *Nat. Commun.* **2021**, *12*, 6513. [[CrossRef](#)]
72. Edge, J.S.; O’kane, S.; Prosser, R.; Kirkaldy, N.D.; Patel, A.N.; Hales, A.; Ghosh, A.; Ai, W.; Chen, J.; Yang, J.; et al. Lithium ion battery degradation: What you need to know. *Phys. Chem. Chem. Phys.* **2021**, *23*, 8200–8221. [[CrossRef](#)]
73. Lee, M.; Han, S.; Park, J.; Kim, J. A Study on the Selection of Failure Factors for Transient State Lithium-Ion Batteries based on Electrochemical Impedance Spectroscopy. *J. Korean Soc. Precis. Eng.* **2021**, *38*, 749–756. [[CrossRef](#)]
74. Iurilli, P.; Brivio, C.; Wood, V. On the use of electrochemical impedance spectroscopy to characterize and model the aging phenomena of lithium-ion batteries: A critical review. *J. Power Sources* **2021**, *505*, 229860. [[CrossRef](#)]
75. Li, Y.; Abdel-Monem, M.; Gopalakrishnan, R.; Berecibar, M.; Nanini-Maury, E.; Omar, N.; van den Bossche, P.; Van Mierlo, J. A quick on-line state of health estimation method for Li-ion battery with incremental capacity curves processed by Gaussian filter. *J. Power Sources* **2018**, *373*, 40–53. [[CrossRef](#)]
76. Hua, Y.; Liu, X.; Zhou, S.; Huang, Y.; Ling, H.; Yang, S. Toward sustainable reuse of retired lithium-ion batteries from electric vehicles. *Resour. Conserv. Recycl.* **2021**, *168*, 105249. [[CrossRef](#)]
77. Waag, W.; Käbitz, S.; Sauer, D.U. Experimental investigation of the lithium-ion battery impedance characteristic at various conditions and aging states and its influence on the application. *Appl. Energ.* **2013**, *102*, 885–897. [[CrossRef](#)]

78. Kang, T.W.; Kim, J.H.; Lee, P.Y.; Ha, M.L.; Song, H.C.; Kim, J.H. Analysis of electrical characteristics of 24S1P battery considering temperature and C-rates. In Proceedings of the KIPE Conference, Hoengseong, Republic of Korea, 3–6 July 2018; pp. 474–475.
79. Vidal, C.; Gross, O.; Gu, R.; Kollmeyer, P.; Emadi, A. xEV Li-ion battery low-temperature effects. *IEEE Trans. Veh. Technol.* **2019**, *68*, 4560–4572. [[CrossRef](#)]
80. Hosseinzadeh, E.; Odio, M.X.; Marco, J.; Jennings, P. Unbalanced performance of parallel connected large format lithium ion batteries for electric vehicle application. In Proceedings of the 2019 International Conference on Smart Energy Systems and Technologies (SEST), Porto, Portugal, 9–11 September 2019; pp. 1–6.
81. Karimi, G.; Li, X. Thermal management of lithium-ion batteries for electric vehicles. *Int. J. Energ. Res.* **2013**, *37*, 13–24. [[CrossRef](#)]
82. Yang, N.; Zhang, X.; Shang, B.; Li, G. Unbalanced discharging and aging due to temperature differences among the cells in a lithium-ion battery pack with parallel combination. *J. Power Sources* **2016**, *306*, 733–741. [[CrossRef](#)]
83. Docimo, D.J.; Fathy, H.K. Analysis and control of charge and temperature imbalance within a lithium-ion battery pack. *IEEE Trans. Control. Syst. Technol.* **2018**, *27*, 1622–1635. [[CrossRef](#)]
84. Oeser, D.; Ziegler, A.; Ackva, A. Single cell analysis of lithium-ion e-bike batteries aged under various conditions. *J. Power Sources* **2018**, *397*, 25–31. [[CrossRef](#)]
85. Wang, T.; Tseng, K.J.; Zhao, J.; Wei, Z. Thermal investigation of lithium-ion battery module with different cell arrangement structures and forced air-cooling strategies. *Appl. Energy* **2014**, *134*, 229–238. [[CrossRef](#)]
86. Zhao, J.; Rao, Z.; Huo, Y.; Liu, X.; Li, Y. Thermal management of cylindrical power battery module for extending the life of new energy electric vehicles. *Appl. Therm. Eng.* **2015**, *85*, 33–43. [[CrossRef](#)]
87. Lee, S.; Kwon, M.; Kim, Y. Preventing Thermal Runaway Propagation in Lithium-ion Batteries using a Passive Liquid Housing. *J. Electrochem. Soc.* **2024**, *171*, 030507. [[CrossRef](#)]
88. Huang, C.K.; Sakamoto, J.S.; Wolfenstine, J.; Surampudi, S. The limits of low-temperature performance of Li-ion cells. *J. Electrochem. Soc.* **2000**, *147*, 2893. [[CrossRef](#)]

**Disclaimer/Publisher’s Note:** The statements, opinions and data contained in all publications are solely those of the individual author(s) and contributor(s) and not of MDPI and/or the editor(s). MDPI and/or the editor(s) disclaim responsibility for any injury to people or property resulting from any ideas, methods, instructions or products referred to in the content.